SIAM J. SCI. COMPUT.
Vol. 36, No. 3, pp. B273–B293

RECONSTRUCTION OF THE REFRACTIVE INDEX FROM EXPERIMENTAL BACKSCATTERING DATA USING A GLOBALLY CONVERGENT INVERSE METHOD*

NGUYEN TRUNG THÀNH†, LARISA BEILINA‡, MICHAEL V. KLIBANOV†, AND MICHAEL A. FIDDY§

Abstract. The problem to be studied in this work is within the context of coefficient identification problems for the wave equation. More precisely, we consider the problem of reconstruction of the refractive index (or equivalently, the dielectric constant) of an inhomogeneous medium using one backscattering boundary measurement. The goal of this paper is to analyze the performance of the globally convergent algorithm of Beilina and Klibanov on experimental data collected using a microwave scattering facility at the University of North Carolina at Charlotte. The main challenge in working with experimental data is the huge misfit between these data and computationally simulated data. We present data preprocessing steps to make the former somehow look similar to the latter. Results of both nonblind and *blind* targets are shown that indicate good reconstructions even for high contrasts between the targets and the background medium.

Key words. coefficient identification, wave equation, globally convergent algorithm, experimental data, data preprocessing

AMS subject classifications. 35R30, 35L05, 78A46

DOI. 10.1137/130924962

1. Introduction.

Microwave imaging technology is widely used to visualize objects and materials that are opaque at visible wavelengths, and it is thus important for inspection, surveillance, and remote sensing from hand-held medical to satellite-borne defense applications; see, e.g., [19]. In this paper, we consider the problem of the reconstruction of the refractive indices (equivalently, the dielectric constants) of unknown targets placed in a homogeneous medium using experimental measurements of time-domain backscattered electromagnetic waves, generated by a single source, in the microwave range. Mathematically speaking, this is a coefficient inverse problem (CIP) for the time-dependent wave-like equation: we reconstruct a spatially varying coefficient of this equation using measurements on a part of the boundary of the domain of interest. Potential applications of this problem are in the detection and characterization of explosives, including improvised explosive devices (IEDs). Note that IEDs are often located above the ground surface [16], which is somewhat close to our case of targets located in air. The case when targets are buried under the ground will be reported in a future publication.

Different migration-type methods have been applied to this type of measurement

*Submitted to the journal's Computational Methods in Science and Engineering section June 14, 2013; accepted for publication (in revised form) January 27, 2014; published electronically May 1, 2014. This research was supported by US Army Research Laboratory and US Army Research Office grants W911NF-11-1-0325 and W911NF-11-1-0399, by the Swedish Research Council, by the Swedish Foundation for Strategic Research (SSF) in the Gothenburg Mathematical Modelling Centre (GMMC), and by the Swedish Institute, Visby Program.

http://www.siam.org/journals/sisc/36-3/92496.html

†Department of Mathematics and Statistics, University of North Carolina at Charlotte, Charlotte, NC 28223 (tnguy152@uncc.edu, mklibanv@uncc.edu).

‡Department of Mathematical Sciences, Chalmers University of Technology and Gothenburg University, SE-42196 Gothenburg, Sweden (larisa@chalmers.se).

§Optoelectronics Center, University of North Carolina at Charlotte, Charlotte, NC 28223 (mafiddy@uncc.edu).

to obtain geometrical information such as the shapes, the sizes, and the locations of the targets; see, e.g., [20, 22]. However, the refractive indices, which characterize the targets in terms of their constituent materials, are much more difficult to estimate. For conventional gradient-based optimization methods, there is a huge literature; see, e.g., [2, 11, 12] and references therein. It is well known that the convergence of these methods is guaranteed only if the starting point of the iterations is chosen to be sufficiently close to the correct solution. This means that they require some a priori information about the targets being found, which is not always available in many practical situations. A different method was proposed in [4, 6, 15, 16], and results were summarized in the book [5]. This method provides a good approximation for the exact coefficient without a priori knowledge of a small neighborhood of this coefficient. Its global convergence has been rigorously proved for an approximate mathematical model; see Theorem 2.9.4 in [5] and Theorem 5.1 in [6]. Due to this model, the method is referred to as an *approximately globally convergent method* (globally convergent method, for short). In [15] the authors demonstrated good reconstruction results for a transmitted experimental data set using this method, whereas a gradient-based method with Tikhonov regularization, starting from the homogeneous medium as the first guess, failed. We also refer to the boundary control method, which was designed to solve a CIP similar to ours, although multiple locations of sources are used; see, e.g., [9].

The goal of this paper is to show how the globally convergent method performs on experimental backscattered data. While previously it was demonstrated how this method works on experimental transmitted data [5, 4, 15], the case of backscattered data is different and much more complicated. Indeed, backscattered signals are much weaker than transmitted ones. In addition, a number of unwanted scattered signals caused by objects present in the room where experiments take place (e.g., furniture) occur in the backscattering case. Although in [16] backscattered data were treated, they were one-dimensional (1-d) data only, while we work here with three-dimensional (3-d) data. To collect these data, an experimental apparatus was built in the Microwave Laboratory at the University of North Carolina at Charlotte, using support from the US Army Research Office.

The main challenge working with our experimental data is a *huge misfit* between these data and computationally simulated ones; see also [5, 4, 15, 16] for the same conclusion. From the functional analysis standpoint this means that the function expressing experimental data is far away in any reasonable norm from the range of the operator of our forward problem. Further, this operator should be inverted in solving the inverse problem. Hence, any inversion algorithm would fail to produce satisfactory results if being applied to the raw data.

Therefore, the *central procedure* before applying the globally convergent algorithm is a heuristic data preprocessing procedure. This procedure makes the experimental data look somewhat similar to the data provided by computational simulations. In other words, it moves the data closer to the range of that operator. The preprocessing procedure of the current paper is substantially different from those of [5, 4, 15, 16] because the data are different, as mentioned above. Moreover, the transmitted data used in [5, 4, 15] were near field measurements, while we consider far field data in this work. Therefore, application of an additional preprocessing step to the data (data propagation) is necessary before using the globally convergent algorithm. We describe our data preprocessing procedure in section 3.

The preprocessed data are used as the input for the globally convergent method.

Our goal is to estimate the refractive indices and the locations of the targets. In addition, we want to estimate sizes of those targets. We should mention that results of this method can be used as initial guesses for locally convergent methods in order to refine images, especially the targets' shapes; see, e.g., [5, 4, 7].

The experimental data sets of this paper include both nonblind and blind cases. "Blind" means that the targets were unknown to the computational team (NTT, LB, MVK) but known to one person (MAF), who was leading the data collection process. Moreover, the refractive indices of these targets were measured after the reconstruction results were obtained. Then computational results were compared with directly measured ones. The nonblind targets were used for the purposes of calibration and fine-tuning of the reconstruction procedure. The blind targets were used to ensure that this procedure works in realistic blind data cases. The same reconstruction procedure, with the same choice of parameters, was used for both types of targets. Our results indicate that we not only accurately reconstruct the refractive indices and the locations of the targets, but also can differentiate between metallic and nonmetallic targets.

2. Problem statement and the globally convergent method. In this section we state the forward and inverse problems under consideration, as well as briefly outline the globally convergent method of [5] for the reader's convenience.

2.1. Forward and inverse problems. As the forward problem, we consider the propagation of the electromagnetic wave in $\mathbb{R}^3$ generated by an incident plane wave. Below, $\mathbf{x} = (x, y, z)$ denotes a point in $\mathbb{R}^3$. Since in our experiments only one component of the electric field E is generated by the source, and since the detector measures only that component of the scattered electric field, we model the wave propagation by the following Cauchy problem for the scalar wave equation:

$$\epsilon(\mathbf{x})u_{tt}(\mathbf{x},t) = \Delta u(\mathbf{x},t) + \delta(z-z_0)f(t), \quad (\mathbf{x},t) \in \mathbb{R}^3 \times (0,\infty), \tag{2.1}$$

$$u(\mathbf{x},0) = 0, \quad u_t(\mathbf{x},0) = 0, \tag{2.2}$$

where u is the total wave generated by the incident plane wave propagating along the z-axis and which is incident at the plane $\{z = z_0\}$. Here $f(t) \not\equiv 0$ is the time-dependent waveform of the incident plane wave. Note that this plane wave model is new for our globally convergent method, since in our previous works the point source was considered, including convergence results mentioned in section 1.

To further justify our use of the single equation (2.1) instead of the full Maxwell's system, we refer to [3], where it was shown numerically that the component of E which was initially incident upon the medium dominates two other components, at least for a rather simple medium such as ours. Besides, a similar scalar equation was successfully used previously to work with transmitted experimental data [5, 4, 7].

In (2.1), $\epsilon(\mathbf{x})$ represents the spatially distributed dielectric constant. We assume that $\epsilon(\mathbf{x})$ is unknown inside a bounded domain $\Omega \subset \mathbb{R}^3$ with $\partial\Omega$ being C^3-regular. In addition, we assume that there exist two positive constants $\epsilon_l \leq 1$ and $\epsilon_u \geq 1$ such that

$$0 < \epsilon_l \leq \epsilon(\mathbf{x}) \leq \epsilon_u \ \forall \mathbf{x} \in \mathbb{R}^3, \qquad \epsilon(\mathbf{x}) \equiv 1 \ \forall \mathbf{x} \notin \Omega. \tag{2.3}$$

In other words, the medium is assumed to be homogeneous outside of Ω. We also assume that the plane where the plane wave is incident is located outside of the domain $\bar{\Omega}$; i.e., $\overline{\Omega} \cap \{z = z_0\} = \varnothing$.

For the theoretical analysis, we state the inverse problem for the case when the data are given at the entire boundary. However, only backscattered data are measured in our experiments. In section 4, we explain how we work with this type of data.

CIP: *Reconstruct the coefficient* $\epsilon(\mathbf{x})$ *for* $\mathbf{x} \in \Omega$*, given the following measured data for a single incident plane wave generated at the plane* $\{z = z_0\}$ *outside of* $\overline{\Omega}$*:*

$$g(\mathbf{x}, t) = u(\mathbf{x}, t), \quad \mathbf{x} \in \partial\Omega, t \in (0, \infty). \tag{2.4}$$

The assumption of the infinite time interval in (2.4) is not a restrictive one, because in our method we apply the Laplace transform to $g(\mathbf{x},t)$ with respect to t. Since the kernel of this transform decays exponentially with respect to t, the Laplace transform effectively cuts off to zero values of the function $g(\mathbf{x},t)$ for large t.

Concerning the uniqueness of this CIP, global uniqueness theorems for multidimensional CIPs with a single measurement are currently known only under the assumption that at least one of the initial conditions does not equal zero in the entire domain $\overline{\Omega}$. All these theorems were proved by the method originated in [10]; see also sections 1.10 and 1.11 in [5] about this method. This technique is based on Carleman estimates. Since both initial conditions (2.2) equal zero in $\overline{\Omega}$, this method is inapplicable to our case. However, since we need to solve our CIP numerically anyway, we assume that uniqueness holds.

We remark that (2.1) is invalid if metallic objects are present in the domain Ω. To deal with this type of target, we follow a suggestion of [16]. It was established numerically in [16] that metals can be modeled as dielectrics with a high dielectric constant, which is referred to as the "appearing" dielectric constant of metals. It is suggested in [16] that this dielectric constant can be chosen as

$$\epsilon\,(\text{metals}) \in [10, 30]\,. \tag{2.5}$$

2.2. The globally convergent method. The globally convergent method of [5] works with the Laplace transformed data. However, we do not invert the Laplace transform. Let

$$\tilde{u}(\mathbf{x}, s) = \int_0^\infty u(\mathbf{x}, t) e^{-st} dt, \tag{2.6}$$

where s is a positive parameter referred to as the *pseudofrequency*. We assume that $s \geq \underline{s} > 0$, where the number $\underline{s}$ is large enough so that the Laplace transforms of u and its derivatives $D^k u$, $k = 1, 2$, converge absolutely. We also denote by $\tilde{f}(s)$ the Laplace transform of $f(t)$. We assume that $\tilde{f}(s) \neq 0$ for all $s \geq \underline{s}$. Define $w(\mathbf{x}, s) := \tilde{u}(\mathbf{x}, s)/\tilde{f}(s)$. The function w satisfies the equation

$$\Delta w(\mathbf{x}, s) - s^2 \epsilon(\mathbf{x}) w(\mathbf{x}, s) = -\delta(z - z_0), \quad \mathbf{x} \in \mathbb{R}^3,\ s \geq \underline{s}. \tag{2.7}$$

Following the same arguments as in the proof of Theorem 2.7.2 of [5], we can prove that $w(\mathbf{x}, s) > 0$ and $\lim_{|\mathbf{x}|\to\infty} [w\,(\mathbf{x}, s) - w_0(\mathbf{x}, s)] = 0$, where $w_0\,(\mathbf{x}, s) := e^{-s|z-z_0|}/\,(2s)$ is such a solution of (2.7) for the case $\epsilon\,(\mathbf{x}) \equiv 1$, which decays to zero as $|z| \to \infty$. Next, define the function v by $v := (\ln w)/s^2$. Substituting $w = e^{vs^2}$ into (2.7) and keeping in mind that $\overline{\Omega} \cap \{z = z_0\} = \varnothing$, we obtain

$$\Delta v + s^2 |\nabla v|^2 = \epsilon(\mathbf{x}), \quad \mathbf{x} \in \Omega. \tag{2.8}$$

Equation (2.8) shows that the coefficient $\epsilon(\mathbf{x})$ can be computed directly via the function v. To compute v, we eliminate the unknown coefficient $\epsilon(\mathbf{x})$ from (2.8) by taking

the derivative with respect to s on both sides of (2.8). Define $q := \partial_s v$. Then

$$v = -\int_s^\infty q d\tau = -\int_s^{\bar{s}} q d\tau + V, \tag{2.9}$$

where $\bar{s} > \underline{s}$, which plays the role of a regularization parameter and is chosen numerically in the computational practice. The function $V(\mathbf{x}) := v(\mathbf{x}, \bar{s})$ is called the "tail function." Note that

$$V(\mathbf{x}) = \frac{\ln w(\mathbf{x}, \bar{s})}{\bar{s}^2}. \tag{2.10}$$

From (2.8) we obtain the following differential integral equation involving q and V:

$$\begin{aligned} &\Delta q - 2s^2 \nabla q \cdot \int_s^{\bar{s}} \nabla q(\mathbf{x}, \tau) d\tau + 2s^2 \nabla V \cdot \nabla q + 2s \left| \int_s^{\bar{s}} \nabla q(\mathbf{x}, \tau) d\tau \right|^2 \\ &- 4s \nabla V \cdot \int_s^{\bar{s}} \nabla q(\mathbf{x}, \tau) d\tau + 2s \left| \nabla V \right|^2 = 0, \qquad \mathbf{x} \in \Omega. \end{aligned} \tag{2.11}$$

It follows from (2.4) that q satisfies the following boundary condition:

$$q(\mathbf{x}, s) = \psi(\mathbf{x}, s), \mathbf{x} \in \partial\Omega, \tag{2.12}$$

where $\psi(\mathbf{x}, s) = \frac{\partial}{\partial s}[\frac{\ln(\varphi)}{s^2}]$ with $\varphi(\mathbf{x}, s) = \int_0^\infty g(\mathbf{x}, t) e^{-st} dt / \tilde{f}(s)$.

Note that (2.11) has two unknown functions, q and V. In order to approximate both of them, we treat them differently. In particular, we use an iterative procedure with respect to the tail function V as described below.

2.3. Discretization and description of the algorithm. Divide the pseudo-frequency interval $[\underline{s}, \bar{s}]$ into N uniform subintervals by $\bar{s} = s_0 > s_1 > \cdots > s_N = \underline{s}$, $s_n - s_{n+1} = h$. We approximate q by $q(\mathbf{x}, s) \approx q_n(\mathbf{x})$, $s \in (s_n, s_{n-1}]$, $n = 1, \ldots, N$. We also set $q_0 \equiv 0$. Then after some manipulations, a system of elliptic equations for functions $q_n(x)$ is derived from (2.11) using the so-called Carleman weight function $\exp[\lambda(s - s_{n-1})]$, $s \in (s_n, s_{n-1})$, where $\lambda \gg 1$ is a certain parameter. We take $\lambda = 20$ in all our computations. This system is

$$\begin{aligned} &\Delta q_n + A_{1,n} \nabla q_n \cdot (\nabla V_n - \nabla \overline{q_{n-1}}) \\ &= A_{2,n} |\nabla q_n|^2 + A_{3,n} \left(|\nabla \overline{q_{n-1}}|^2 + |\nabla V_n|^2 - 2 \nabla V_n \cdot \nabla \overline{q_{n-1}} \right), \end{aligned} \tag{2.13}$$

where $A_{i,n}$, $i = 1, 2, 3$, are some coefficients, depending on s_n and λ, which are analytically computed, and $\nabla \overline{q_{n-1}} = h \sum_{j=0}^{n-1} \nabla q_j$. Here we indicate the dependence of the tail function $V := V_n$ on the number n, because we approximate V iteratively. The discretized version of the boundary condition (2.12) is given by

$$q_n(\mathbf{x}) = \psi_n(\mathbf{x}) := \frac{1}{h} \int_{s_n}^{s_{n-1}} \psi(\mathbf{x}, s) ds \approx \frac{1}{2} [\psi(\mathbf{x}, s_n) + \psi(\mathbf{x}, s_{n-1})], \quad \mathbf{x} \in \partial\Omega. \tag{2.14}$$

One can prove that $|A_{2,n}| \leq C/\lambda$ for sufficiently large λ, where $C > 0$ is a certain constant. Hence, the first term on the right-hand side of (2.13) is dominated by the other terms. Therefore, in the following we set $A_{2,n} |\nabla q_n|^2 := 0$. The system of elliptic equations (2.13) with boundary conditions (2.14) can be solved sequentially starting from $n = 1$. To solve it, we make use of the iterative process: for a given n and some approximation $q_{n,i-1}$ of q_n we find the next approximation $q_{n,i}$ of q_n by solving (2.13)–(2.14). Denote by m_n the number of these iterations. The full algorithm is described as follows.

Globally convergent algorithm.

- Given the first tail V_0. Set $q_0 \equiv 0$.
- For $n = 1, 2, \ldots, N$:
  1. Set $q_{n,0} = q_{n-1}$, $V_{n,1} = V_{n-1}$.
  2. For $i = 1, 2, \ldots, m_n$:
     - Find $q_{n,i}$ by solving (2.13)–(2.14) with $V_n := V_{n,i}$.
     - Compute $v_{n,i} = -hq_{n,i} - \overline{q_{n-1}} + V_{n,i}$, $\mathbf{x} \in \Omega$.
     - Compute $\epsilon_{n,i}$ via (2.8). Then solve the forward problem (2.1)–(2.2) with the new computed coefficient $\epsilon := \epsilon_{n,i}$, compute $w := w_{n,i}$, and update the tail $V_{n,i+1}$ by (2.10).
  3. Set $q_n = q_{n,m_n}$, $\epsilon_n = \epsilon_{n,m_n}$, $V_n = V_{n,m_n+1}$ and go to the next frequency interval $[s_{n+1}, s_n]$ if $n < N$. If $n = N$, then stop.

Stopping criteria of this algorithm with respect to i, n should be addressed computationally; see details in section 4.

2.4. The initial tail function and the global convergence. We remark that the convergence of this algorithm depends on the choice of the initial tail function V_0. In [5] (see also [6]) the global convergence of this algorithm was proved within the context of an approximate mathematical model for the case of the point source. Let us recall some results for this case. For the proof of global convergence, we assume that $\epsilon \in C^3(\mathbb{R}^3)$. It was proved in [5] that under some conditions there exists a function $p(\mathbf{x})$ belonging to the Hölder space $C^{2+\alpha}\left(\overline{\Omega}\right)$ such that $V(\mathbf{x}, s) = p(\mathbf{x})/s + O\left(1/s^2\right)$, $s \to \infty$. Due to this asymptotic behavior, we assume that the exact tail is given by

$$V(\mathbf{x}, s) = \frac{p(\mathbf{x})}{s} = \frac{\ln w(\mathbf{x}, s)}{s^2} \qquad \forall s \geq \overline{s}. \tag{2.15}$$

Note that we use this assumption only on the initializing iteration to obtain $V_0(\mathbf{x})$. Under this assumption, it follows from (2.11), (2.12) that $p(\mathbf{x})$ satisfies

$$\Delta p(\mathbf{x}) = 0, \quad \mathbf{x} \in \Omega, \qquad p \in C^{2+\alpha}\left(\overline{\Omega}\right), \tag{2.16}$$

$$p|_{\partial\Omega} = -\overline{s}^2 \psi(\mathbf{x}, \overline{s}). \tag{2.17}$$

As the first guess for the tail function we take

$$V_0(\mathbf{x}) := \frac{p(\mathbf{x})}{\overline{s}}, \quad \mathbf{x} \in \Omega. \tag{2.18}$$

With this choice of the initial tail function, it was proved in [5, 6] that the proposed algorithm, for the case of the point source, is convergent in the following sense: it delivers some points in a sufficiently small neighborhood of the exact coefficient $\epsilon(\mathbf{x})$. The latter is sufficient for computational purposes. The size of this neighborhood depends on the noise in the data, the discretization step size h, and the domain Ω. We note that no a priori information about the unknown coefficient is used here. Therefore, we say that the algorithm is globally convergent within the framework of the approximation (2.15).

For the case of the incident plane wave, i.e., the model (2.1)–(2.2), we believe that the global convergence of the proposed algorithm can be proved similarly to the case of the point source. A complete proof will be investigated in a future work.

2.5. Numerical solution of the forward problem. Since it is impossible to solve the problem (2.1)–(2.2) in the entire space, in numerical computations we

approximate it by a problem in a bounded domain $G \subset \mathbb{R}^3$ such that $\Omega \subset G$. For simplicity, we choose G as the prism

$$G := \{\mathbf{x} \in \mathbb{R}^3 : X_l \le x \le X_u, Y_l \le y \le Y_u, Z_l \le z \le Z_u\}.$$

We define $\partial G_z^l := \{z = Z_l\}$, $\partial G_z^u := \{z = Z_u\}$, and $\partial G_{xy} = \partial G \setminus (\partial G_z^l \cup \partial G_z^u)$. Here we choose $Z_u = z_0$; i.e., the incident plane wave is generated at the plane ∂G_z^u and propagates in the negative z-direction. Moreover, in our analysis, we assume that the incident wave is excited for a short time period $(0, t_1)$. As a result, the total wave vanishes after a finite time. Therefore, we rewrite the model (2.1)–(2.2) in G as

$$\epsilon(\mathbf{x}) u_{tt}(\mathbf{x}, t) = \Delta u(\mathbf{x}, t), \qquad (\mathbf{x}, t) \in G \times (0, T), \tag{2.19}$$

$$u(\mathbf{x}, 0) = 0, \quad u_t(\mathbf{x}, 0) = 0, \quad \mathbf{x} \in G. \tag{2.20}$$

We now complement (2.19), (2.20) with boundary conditions at the boundary of G. To represent the incident plane wave on ∂G_z^u, we assume that the excitation time $(0, t_1)$ of the incident wave is so small that the incident wave has not yet reached the domain Ω at $t = t_1$. Consequently, $u(\mathbf{x}, t) = u^i(\mathbf{x}, t)$ for $t \le t_1$, where u^i is the incident wave. Note that u^i is a 1-d wave, generated by the source term $\delta(z - z_0) f(t)$, propagating along the z-axis. It can be shown that $\partial_z u^i\big|_{z=Z_u} = f(t)/2$. Hence,

$$\partial_\nu u = f(t)/2, \qquad (\mathbf{x}, t) \in \partial G_z^u \times (0, t_1), \tag{2.21}$$

where ν is the outward normal vector of ∂G. The waveform function f is chosen by $f(t) = 2\omega \cos(\omega t)$, $0 \le t \le t_1 = 2\pi/\omega$, where ω is the angular frequency of the incident plane wave. We also use the following boundary conditions:

$$\partial_\nu u = -u_t, \quad (\mathbf{x}, t) \in \partial G_z^u \times (t_1, T), \tag{2.22}$$

$$\partial_\nu u = -u_t, \quad (\mathbf{x}, t) \in \partial G_z^l \times (0, T), \tag{2.23}$$

$$\partial_\nu u = 0, \quad (\mathbf{x}, t) \in \partial G_{xy} \times (0, T). \tag{2.24}$$

This means that we use the first order absorbing boundary condition at the plane ∂G_z^l as well as at the plane ∂G_z^u for $t > t_1$; see, e.g., [13]. The Neumann boundary condition (2.24) at the lateral boundary ∂G_{xy} allows us to approximately assume that we have an infinite domain in the lateral directions.

The forward problem (2.19)–(2.24) is solved using the software package WavES [21] via the hybrid FEM/FDM method described in [8].

3. The experimental setup and data preprocessing.

3.1. Data acquisition. Our experimental configuration is shown in Figure 1. The setup of our measurements included a horn antenna (transmitter) fixed at a given position and a detector scanning in a square of a vertical plane, which we refer to as the measurement plane. Consider the Cartesian coordinate system $Oxyz$, as shown in Figure 1(b). The scanning area was 1 m by 1 m with a step size of 0.02 m, starting at $(x, y) = (-0.5, -0.5)$ and ending at $(x, y) = (0.5, 0.5)$.

Due to some technical difficulties with the mechanical scanning system, the horn antenna was not placed behind but in front of the measurement plane (between the measurement plane and the targets). Therefore a small area in the center of the scanning area on the measurement plane was shaded by the horn, making the data in that area unreliable. The horn was placed at the distance of about 0.2–0.25 m from

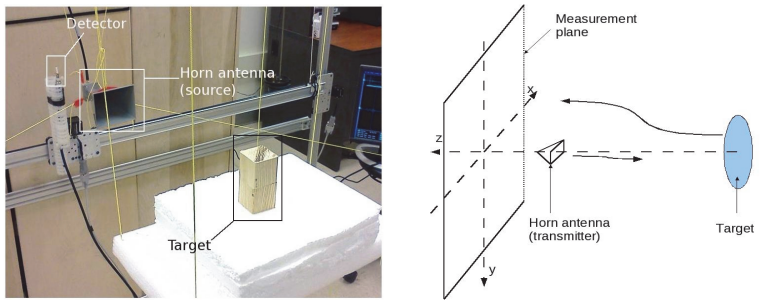

FIG. 1. (a) *A picture of our experiment setup.* (b) *Diagram of our setup.*

the measurement plane, and the distances from the targets to the measurement plane are about 0.8 m.

At each position of the detector, a number of electric pulses were emitted by the horn. The detector received two types of signals: the direct signals from the source and the backscattered signals from the targets and other surrounding objects. The direct signals are used for time reference in data preprocessing. To reduce the instability of the measured signals in terms of their magnitudes, the measurements were repeated 800 times at each detector position, and the average of the recorded time-dependent signals was taken as the measured data at that detector position. Note that this averaging was done during the data acquisition, i.e., before the data preprocessing. By scanning the detector and repeating the measurements, we obtained essentially the same signals as using one incident signal and multiple detectors at the same time.

Pulses were generated by a Picosecond Pulse Generator 10070A. The scattered signals were measured by a Tektronix DSA70000 series real-time oscilloscope. The emitted pulses were of 300 picoseconds duration. The wavelength of the incident pulses was about 0.04 m. The time step between two consecutive records was $\Delta t = 10$ ps. Each signal was recorded for 10 ns.

Since the source is located far away (at about 15 wavelengths) from the targets, the use of the incident plane wave in our model (2.1)–(2.2) is well suited.

3.2. Data preprocessing. One of the biggest challenges in working with these experimental data is to deal with the *huge misfit* between these data and the data produced via computational simulations; also see [5, 4, 15, 16] for the same conclusion. There are several causes of this misfit such as (i) the instability of the amplitude of the emitted signals (incident waves), which causes instability of the received signals; (ii) unwanted waves scattered by several existing objects around our devices (see Figure 2(a)); (iii) the shadow on the measurement plane caused by the transmitting horn antenna; and (iv) the difference between the experimental and simulated incident waves. Figure 3 compares the Laplace transform of an experimental scattered wave and the corresponding simulated one, showing a huge misfit between them. Note that the Laplace transform of the experimental wave was carried out after removing the incident wave and unwanted parts, as shown in Figure 2(c).

Therefore, the *central procedure* required before applying inversion methods is data preprocessing. This procedure is usually heuristic and cannot be rigorously justified. Our data preprocessing consists of six steps, described below. We do not describe Steps 1–3 in detail here, since they are straightforward.

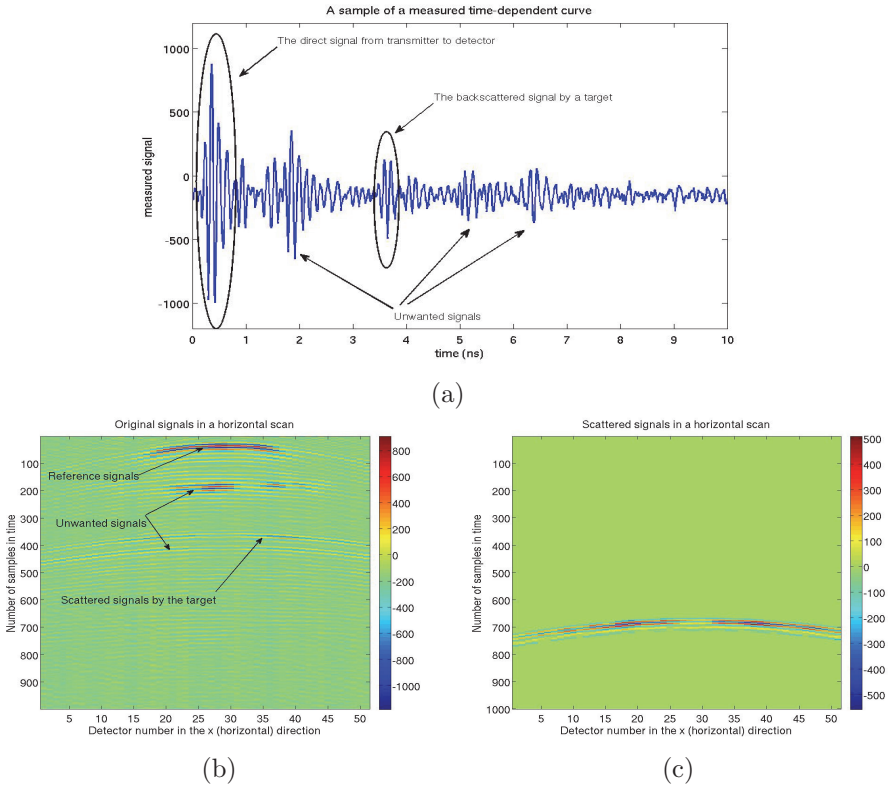

FIG. 2. *An experimental data set:* (a) *a* 1*-d curve,* (b) 2*-d data on a horizontal scan,* (c) *after Steps* 1–4 *of the data preprocessing.*

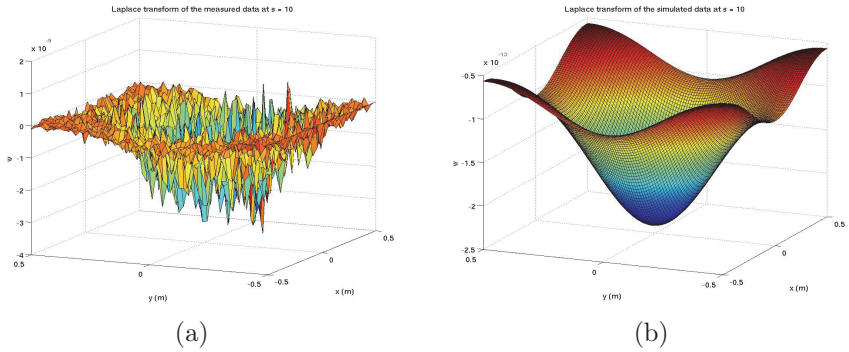

FIG. 3. *Experimental vs. simulated scattered waves on the measurement plane after Laplace transform:* (a) *measured data,* (b) *simulated data.*

Step 1. *Offset correction.* The acquired signals are usually shifted from the zero mean value. This can be corrected by subtracting the mean value from them.

Step 2. *Time-zero correction.* Time-zero refers to the moment at which the signal is emitted from the transmitter. The recorded signals may be shifted in time. We use the direct signals from the transmitter to the detector to correct the time-zero.

Step 3. *Source shift.* As mentioned above, the horn antenna in our experiments is placed between the targets and the measurement plane. However, in data calibration, we need to simulate the data for the case when the measurement plane is between the horn and the targets. Therefore, we artificially "shift" the horn in the positive z-direction such that it is 0.4 m further than the measurement plane from the targets. This is done by shifting the whole time-dependent data by a number of samples which corresponds to the shifted distance.

Step 4. *Extraction of scattered signals.* Apart from the signals backscattered by the targets, our measured data also contain various types of signals as mentioned above. What we need, however, is the signals scattered by the targets only. The extraction of these scattered signals for each target is done as follows. First, we exclude the direct signals and the unwanted signals, which come earlier than the signals scattered by the target (see Figure 2(a)–(b)), by calculating the time of arrival. These unwanted signals are due to the reflection of the direct signals by the metallic structure behind the measurement plane, so we can estimate their times of arrival, as we know the distance from the measurement plane to this structure. Then, as we observed that the signals scattered by the target are the strongest peaks of the remaining data, we first determine, for each detector position, the strongest negative peak after removing the aforementioned signals. Then the signals scattered by the target are taken as seven peaks (four negative peaks and three positive peaks), starting from the first negative peak prior to the strongest one if its amplitude is less than 80% that of the strongest one (see Figure 2(a)). Otherwise, we start from the second negative peak prior to the strongest one. The reason for choosing seven peaks for the scattered signals is the fact that the incident pulses also contain seven strong peaks. We have observed in our computational simulations that if we choose the negative peak as the first peak of the target's signals, we obtain a dielectric constant of the target larger than that of the background. Conversely, if we choose the positive peak as the first peak of the target's signals, the obtained dielectric constant of the target is less than that of the background. Since our targets were placed in air, they should have larger dielectric constants than that of the background. Therefore, we chose as the first peak of the target's signals the negative one. Moreover, we also chose $\epsilon_l = 1$.

Step 5. *Data propagation.* After getting the scattered signals, the next step of data preprocessing is to propagate the data closer to the targets, i.e., to approximate the scattered waves on a plane closer to the targets, compared to the measurement plane. There are two reasons for doing this. The first is that since the kernel of the Laplace transform decays exponentially in terms of the time delay, which is proportional to the distance from the targets to the measurement plane, then the amplitude of the data after the Laplace transform on the measurement plane is very small and can be dominated by the computational error. The second reason is that this propagation procedure helps to reduce the computational cost substantially as the computational domain Ω is reduced. We have also observed that the data propagation helps to reduce the noise in the measured data.

Step 6. *Data calibration.* Finally, since the amplitudes of the experimental incident and scattered waves are usually quite different from those in simulations, we need to scale the former to better match the latter in amplitude. This is done using a known target referred to as the *calibrating object.*

Figure 2 shows an original data set and data after Steps 1–4 for a horizontal scan of the detector. One can see that Steps 1–4 help to remove the unwanted signals. In the following, we present our methods for Steps 5 and 6 in more detail.

3.2.1. Data propagation. Denote by P_m the measurement plane, and by P_p the propagation plane, which is closer to the targets than P_m. Without loss of generality we define $P_m = \{z = a\}$ and $P_p = \{z = 0\}$, where the number $a > 0$. Moreover, denote by $\Gamma = (-0.5, 0.5) \times (-0.5, 0.5)\} \subset \mathbb{R}^2$ the scanning area of the detector on the plane P_m. Let $\Gamma_m = \{(x, y, a) \in \mathbb{R}^3 : (x, y) \in \Gamma\}$ and $\Gamma_p = \{(x, y, 0) \in \mathbb{R}^3 : (x, y) \in \Gamma\}$. We also denote by $u^s(\mathbf{x}, t)$ the scattered wave. Note that the medium between P_m and P_p is homogeneous with $\epsilon = 1$, and the scattered wave u^s propagates in the direction from P_p to P_m. The aim of the data propagation is to approximate $u^s\big|_{\Gamma_p \times (0,\infty)}$ from the measured data $\widetilde{g}(x, y, t) := u^s\big|_{\Gamma_m \times (0,\infty)}$.

To do this, we make use of a time reversal method. Its idea is to reverse the scattered wave in time via solution of an initial boundary value problem for the time-reversed wave function. We proceed as follows.

Since short pulses are used as incident waves, it is reasonable to assume that the scattered wave u^s in the domain between P_m and P_p vanishes along with its time derivative u^s_t after some time T. Therefore in the following we consider only the finite time interval $(0, T)$. Denote $\tau := T - t$. Then the time-reversed wave function $u^r(\mathbf{x}, \tau) := u^s(\mathbf{x}, t)$ satisfies the homogeneous wave equation. Moreover, it propagates in the negative z-direction, i.e., from P_m to P_p. To find $u^r\big|_{\Gamma_p}$, we consider the domain $D := \{\mathbf{x} \in \mathbb{R}^3 : (x, y) \in \Gamma, b < z < a\}$ with $b < 0$. Note that $\Gamma_p \subset D$. The reason for choosing this larger domain is that we need to assign boundary conditions at ∂D. Indeed, we assume that u^r satisfies the absorbing boundary condition at $\Gamma_b := \{(x, y, b) : (x, y) \in \Gamma\}$. On Γ_b, far from our propagation plane, this boundary condition means, heuristically, that we "send back" the original scattered wave u^s recorded at P_m. On the other hand, we impose the zero Neumann boundary condition at the rest of the boundary of D, except at Γ_m. Define $Q_T = D \times (0, T)$ and $\Gamma_3 := \partial D \setminus (\Gamma_m \cup \Gamma_b)$. We obtain the following problem for the function $u^r(\mathbf{x}, \tau)$:

$$u^r_{\tau\tau} = \Delta u^r, \quad (\mathbf{x}, \tau) \in Q_T, \tag{3.1}$$

$$u^r(\mathbf{x}, 0) = u^r_\tau(\mathbf{x}, 0) = 0, \quad \mathbf{x} \in D, \tag{3.2}$$

$$u^r\big|_{\Gamma_m \times (0,T)} = \widetilde{g}(x, y, T - \tau), \tag{3.3}$$

$$(\partial_\nu u^r + \partial_\tau u^r)\big|_{\Gamma_b \times (0,T)} = 0, \tag{3.4}$$

$$\partial_\nu u^r\big|_{\Gamma_3 \times (0,T)} = 0. \tag{3.5}$$

A similar procedure was proposed and numerically implemented for computationally simulated data in [1]. However, the absorbing boundary condition for the original scattered wave u^s was applied in [1]. Since our time-reversed wave function u^r propagates from Γ_m to Γ_b, we believe that it is more natural to apply the absorbing boundary condition on Γ_b to u^r. We refer the reader to [14, 18] and the references therein for the experimental time reversal mirror method, a similar procedure but using a physical mirror to reverse the received signals in time and send them back to the targets. Note that we do not locate scatterers in this data propagation procedure as done by the above references or by the time reversal method for detecting small scatterers using multistatic measurements.

Theorem 3.1 below shows the stability of the problem (3.1)–(3.5). For brevity we are not concerned here with minimal smoothness assumptions and leave aside the question of existence, which we conjecture can be addressed via the technique of Chapter 4 of [17].

THEOREM 3.1. *Assume that there exists a solution $u^r \in H^2(Q_T)$ of the problem*

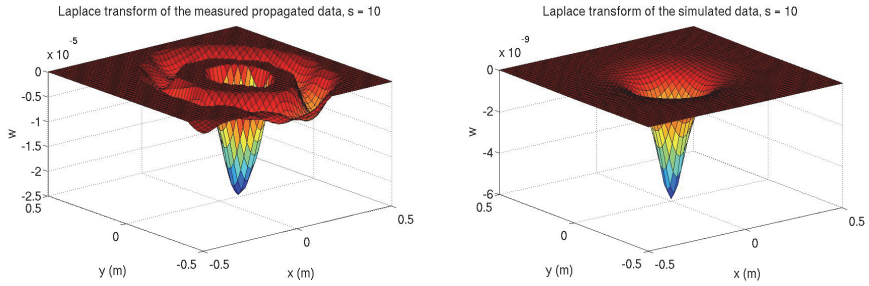

(a) (b)

FIG. 4. *Laplace transform of the scattered wave on the propagation plane P_p:* (a) *measured data,* (b) *simulated data.*

(3.1)–(3.5). *Also, assume that the function $\widetilde{g} \in H^2(\Gamma_m \times (0,T))$ and there exists such a function $F \in H^2(Q_T)$ that*

$$F(\mathbf{x},0) = F_\tau(\mathbf{x},0) = 0, \quad (\partial_\nu F + F_\tau)\,|_{\Gamma_b \times (0,T)} = 0, \quad \partial_\nu F\,|_{\Gamma_3 \times (0,T)} = 0, \tag{3.6}$$

$$F\,|_{\Gamma_m \times (0,T)} = \widetilde{g}(\mathbf{x},t), \quad \|F\|_{H^2(Q_T)} \leq C\,\|\widetilde{g}\|_{H^2(\Gamma_m \times (0,T))}, \tag{3.7}$$

where $C > 0$ is a certain number. Then that solution u^r is unique, and the following stability estimate holds with a constant $C_1 = C_1(C, Q_T) > 0$ depending only on the listed parameters:

$$\|u^r\|_{H^1(Q_T)} \leq C_1\,\|\widetilde{g}\|_{H^2(\Gamma_m \times (0,T))}. \tag{3.8}$$

The proof of Theorem 3.1 is given in the appendix. We note that this theorem can be extended to more general domains and to a general hyperbolic equation.

By solving (3.1)–(3.5), we obtain an approximation of $u^r(\mathbf{x},\tau)$ and then obtain an approximation of u^s for $\mathbf{x} \in \Gamma_p$. In this work, we use the finite difference method to solve this problem. We note that other methods can also be used to solve this data propagation problem such as the Fourier transform method or the quasi-reversibility method. We will discuss these two methods in future works.

3.2.2. Data calibration. Usually the experimental data have quite different amplitudes than do the simulations; see Figure 4, which shows that the minimum of the Laplace transform of the propagated measured data is approximately -2×10^{-5}, whereas the minimum of the simulated data is about -5×10^{-9}. We choose a number, which is called *calibration factor,* to scale the measured data to the same scaling as in our simulations. To do this, we make use of the measured data of a single calibrating object whose location, shape, size, and material are known. The word "single" is important here to ensure that the calibration procedure is unbiased; i.e., it remains the same for all targets.

First, we computationally simulate the data on Γ_p for the calibrating object by solving the problem (2.19)–(2.24). Next, we compute the Laplace transform (2.6) of this computationally simulated solution. Just as in [5], in studies below we work with $s \in [\underline{s}, \overline{s}]$. Numbers $\underline{s}, \overline{s}$ are chosen numerically; see section 4. Denote by $w^t_{sim}(\mathbf{x},s)$, $w^s_{sim}(\mathbf{x},s)$, and $w^i_{sim}(\mathbf{x},s)$, respectively, the Laplace transforms of the total wave, the scattered wave, and the incident wave of the simulated solution for the calibrating object. Clearly, $w^s_{sim}(\mathbf{x},s) = w^t_{sim}(\mathbf{x},s) - w^i_{sim}(\mathbf{x},s)$. It can be proved that $w^s_{sim}(\mathbf{x},s) \leq 0$; see Figure 4(b). Figure 4(b) displays the function $w^s_{sim}(\mathbf{x},s)$ for

$\mathbf{x} \in \Gamma_p$, and qualitatively this is a typical behavior for all targets. Let

$$d_{sim,s} = \min_{\Gamma_p} w^s_{sim}(\mathbf{x}, s).$$

Next, for $\mathbf{x} \in \Gamma_p$ let $w^s_{exp}(\mathbf{x}, s)$ be the Laplace transform of the propagated experimental data for the calibrating object; see Figure 4(a). Define

$$d_{exp,s} = \min_{\Gamma_p} w^s_{exp}(\mathbf{x}, s).$$

The number $d_{sim,s}/d_{exp,s}$ is used as the calibration factor for all targets at pseudofrequency s. That means that the propagated measured data of all targets are multiplied by this calibration factor before being used in the inversion algorithm.

For the data sets used in this paper, we have two types of targets: dielectric and metallic targets. We have observed that two different calibration factors should be used for these two types of targets, because the signals from them have different levels of amplitude. First, we differentiated these two types of targets by comparing the amplitudes of the recorded signals. Indeed, we have consistently observed that the maximal values of amplitudes of measured signals are at least two times larger for metallic targets than for dielectric ones on those positions of detectors which are most sensitive to the presence of targets. Next, we chose in each type a known object as the calibrating object. In other words, we should use a dielectric calibrating object for all dielectric targets and another metal calibrating object for all metallic targets.

The value of $\epsilon(\mathbf{x})$ for the dielectric calibrating object was taken as $\epsilon(\mathbf{x}) = 4.28$ inside that target and $\epsilon(\mathbf{x}) = 1$ outside of it. For the metallic calibrating object, as suggested by (2.5), we took $\epsilon(\mathbf{x}) = 12$ inside and $\epsilon(\mathbf{x}) = 1$ outside of it.

4. Numerical implementation and reconstruction results. Now we describe some details of the numerical implementation and present reconstruction results for our experimental data using the globally convergent algorithm. In our computations, the frequency of the simulated incident wave was chosen as $\omega = 30$.

There were ten data sets tested in this paper. Each data set consisted of only one target, numbered from 1 to 10. Four of them (targets 1–4) were nonblind, and six of them (targets 5–10) were blind. In our data preprocessing, we chose target 1 (a piece of wood) and target 3 (a metallic sphere) as our calibrating objects.

4.1. Dimensionless variables. The spatial dimensions in our experiment were given in meters. Since the scanning step in our measured data was 0.02 m in both x- and y-directions, we chose the dimensionless spatial variable $\mathbf{x}'$ to be $\mathbf{x}' = \mathbf{x}/1(m)$. Next, to scale the wave speed to be 1 in the homogeneous medium, as in our simulations, we chose the dimensionless time t' by $t' = 0.3t$, where t is the time given in nanoseconds (ns). The factor 0.3 is the speed of light in m/ns in free space. For simplicity of notation, we use $\mathbf{x}$ and t again to denote the dimensionless variables.

4.2. Choosing the domains. Before applying the inversion algorithm, some information about the targets was in place already from the measured data due to the data preprocessing. First, we obtained the distance from the targets to the measurement plane. Second, by the data propagation, the targets' locations in the xy plane were estimated. Third, we also differentiated between nonmetallic and metallic targets directly from the measured data based on signal amplitudes.

Given the estimated distances from the targets to the measurement plane, which were about 0.8 m, we propagated the measured data from the measurement plane

$P_m = \{z = 0.8\}$ to the plane $P_p = \{z = 0.04\}$. This means that the distance from the front sides of the targets to the backscattering boundary of our inversion domain was about 0.04 m. The reason for choosing this distance was due to good reconstruction results we have obtained for several nonblind targets. The domain Ω was chosen by

$$\Omega = \{\mathbf{x} \in (-0.5, 0.5) \times (-0.5, 0.5) \times (-0.1, 0.04)\}. \tag{4.1}$$

For solving the forward problem (2.19)–(2.24), using a hybrid of the finite difference method (FDM) and the finite element method (FEM), we chose the domain G as

$$G = \{\mathbf{x} \in (-0.56, 0.56) \times (-0.56, 0.56) \times (-0.16, 0.1)\}.$$

This domain G was decomposed into two subdomains: $G = \Omega \cup (G \setminus \Omega)$. We recall that $\epsilon(\mathbf{x}) = 1$ in $G \setminus \Omega$. Therefore, it is only necessary to solve the inverse problem in Ω. In Ω we use an FEM mesh with tetrahedral elements, while in $G \setminus \Omega$ we use an FDM mesh with the mesh size of 0.02 by 0.02 by 0.02 in Test 1 and 0.01 by 0.01 by 0.01 in Test 2 below. The reason for using the FEM mesh in Ω is that it is possible to refine the reconstruction using adaptive mesh refinement. However, we do not discuss this step in this work. We refer to [5, 7] for more details about the adaptivity.

The time interval $(0, T)$ in the forward problem (2.19)–(2.24) was chosen equal to $(0, 1.2)$. Since the explicit scheme in time was used in WaveES [21], the time step size was chosen as $\Delta t = 0.0015$, which satisfies the CFL stability condition.

The pseudofrequencies s_n were chosen from $\underline{s} = 8$ to $\overline{s} = 10$ with the step size $h = 0.05$. This frequency interval was chosen because it gave good reconstructions of the nonblind targets.

4.3. Estimation of the *xy* projection. During our data preprocessing for nonblind targets, we observed that the xy projection of a target can be roughly estimated directly from the propagated data. Indeed, we define Γ_T as

$$\Gamma_T = \{(x, y) : v_{prop}(x, y, \bar{s}) < 0.85 \min v_{prop}(x, y, \bar{s})\}, \tag{4.2}$$

where v_{prop} is the function v which is constructed from the propagated measured data on the propagation plane Γ_p. Note that the function v_{prop} has a negative peak corresponding to each target; see Figure 4. The truncation value 0.85 was chosen based on trial-and-error tests on some nonblind targets with known sizes. We observed that Γ_T provided a good approximation for the xy projection of a target. Note that the same truncation was applied to blind targets as well. Hence, it is not biased.

Figure 5 shows the estimated xy projections of targets 4 and 10 in our experiments; see Table 1. Although the corners of the targets are not well estimated, we see that their shapes and sizes are reasonably good. For target 10, since its lower part was filled with the sand and the upper part was air inside of a wooden cover (see section 4.7 for details), we can see only the lower part due to its higher refractive index compared to the upper part.

4.4. Completing backscattered data. We recall that only backscattered signals were measured in our experiments. This means that after data propagation, the function $\psi(\mathbf{x}, s)$ was known only on the side $\Gamma_p = \{\mathbf{x} \in \partial\Omega : |x|, z = 0.04\}$ of Ω. As in [6], we replace the missing data on the other parts of $\partial\Omega$ by the corresponding solution of the forward problem in the homogeneous medium. In other words, in our computations, the function ψ is given by

$$\psi(\mathbf{x}, s) = \begin{cases} \psi_{prop}(\mathbf{x}, s), & \mathbf{x} \in \Gamma_p, s \in (\underline{s}, \bar{s}), \\ \psi^i_{sim}(\mathbf{x}, s), & \mathbf{x} \in \partial\Omega \setminus \Gamma_p, s \in (\underline{s}, \bar{s}), \end{cases} \tag{4.3}$$

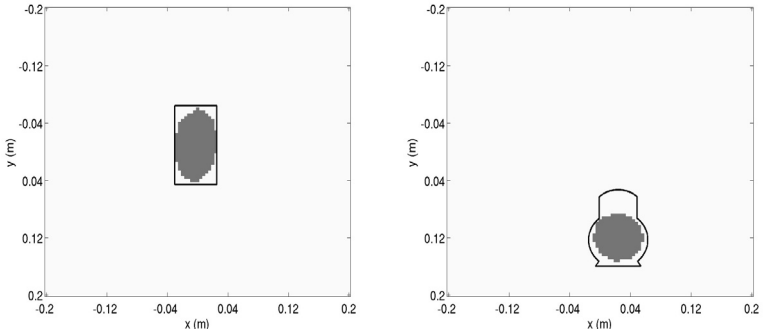

FIG. 5. *Estimation of target's xy projection:* (a) *target* 4 *(a metallic cylinder),* (b) *target* 10 *(a wooden doll partly filled with sand). Thin lines indicate boundaries of correct xy projections.*

TABLE 1
Computed and measured refractive indices of six dielectric targets. The average error in direct measurements is 24%. *The average error of Test* 1 *is* 8% *and Test* 2 *is* 3.4%.

Target ID	1	2	5	8	10
Blind/nonblind (yes/no)	No	No	Yes	Yes	Yes
Measured value, error	2.11, 19%	1.84, 18%	2.14, 28%	1.89, 30%	2.1, 26%
n^{comp} Test 1, error	1.92, 10%	1.80, 2%	1.83, 17%	1.86, 2%	1.92, 9%
n^{comp} Test 2, error	2.03, 4%	1.96, 7%	2.10, 2%	1.85, 2%	2.05, 2%

TABLE 2
Computed "appearing" dielectric constants ϵ^{comp} *of metallic targets.*

Target ID	3	4	6	7	9
Blind/nonblind (yes/no)	No	No	Yes	Yes	Yes
ϵ^{comp} Test 1	14.37	16.93	25.0	13.61	13.56
ϵ^{comp} Test 2	7.59	10.76	19.55	8.12	7.89

where ψ_{prop} is computed from the propagated measured data at Γ_p and ψ^i_{sim} is computed from the simulated solution of the problem (2.19)–(2.24) with $\epsilon(\mathbf{x}) \equiv 1$ in the wave equation (2.19). In the following, we also denote by $V_{prop}(\mathbf{x}) := v_{prop}(x, y, \bar{s})$, $\mathbf{x} \in \Gamma_p$, $s \in [\underline{s}, \bar{s}]$, the tail function (2.10) of the propagated measured data.

We remark that this method of data completion is a heuristic one, and it was found in [6] that it works well for computationally simulated data with the inclusion/background contrast of either 4 or 25. Furthermore, as shown in the results below, it also works well for the experimental data considered in the current paper for contrasts in ϵ varying between 3.24 and 25 (see Tables 1 and 2). Note that Table 1 represents $n = \sqrt{\epsilon}$. Of course, other data completion methods may also be applied.

Below we present the reconstruction results of two different tests: Test 1 and Test 2. In Test 1, we made use of the first tail function computed from the boundary value problem (2.16)–(2.17). As was remarked in section 2.4, global convergence with this choice of the initial tail function is rigorously guaranteed. In Test 2, we choose the first tail function from some information about the targets which we obtained in the data preprocessing. Although the convergence of the resulting algorithm has not been rigorously proved yet, our numerical results show good reconstructions. As we mentioned in section 2.3, stopping criteria of the algorithm should be addressed

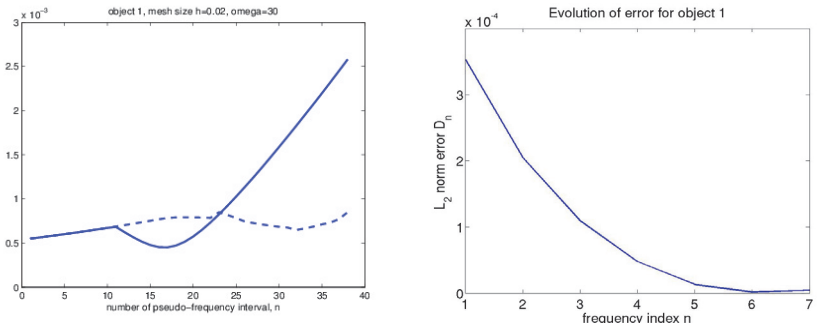

(a) (b)

FIG. 6. (a) *Behavior of the norms* $D_{n,first}$ *(solid curve) and* $D_{n,final}$ *(dash curve) of Test* 1. (b) *Behavior of* $D_{n,final}$ *of Test* 2.

numerically. We will discuss this in what follows.

4.5. Test 1. When testing the algorithm for different nonblind targets in this test, we have developed a reliable stopping criterion which includes two steps.

Stopping criterion for inner iterations with respect to i. The inner iterations are stopped at $i = m_n$ such that either (4.4) or (4.5) is fulfilled,

$$E_{n,i} \geq E_{n,i-1} \quad \text{or} \quad E_{n,i} \leq \eta, \tag{4.4}$$

$$D_{n,i} \geq D_{n,i-1} \quad \text{or} \quad D_{n,i} \leq \eta, \tag{4.5}$$

where $\eta = 10^{-6}$ is a chosen tolerance and $D_{n,i} = ||V_{n,i}|_{\Gamma_p} - V_{prop}||_{L_2(\Gamma_p)}$. In (4.4), $E_{n,i}$ represents the relative error of the coefficient, which is given by

$$E_{n,i} = \frac{||\epsilon_{n,i} - \epsilon_{n,i-1}||_{L_2(\Omega)}}{||\epsilon_{n,i-1}||_{L_2(\Omega)}}.$$

Criterion for choosing the final coefficient. In Test 1, the inversion algorithm was run for all pseudofrequencies in the chosen interval $s \in [8, 10]$, and then the final reconstructed coefficient was chosen as follows. On every pseudofrequency interval $[s_n, s_{n-1})$ we took the norms $D_{n,first} = D_{n,1}$ and $D_{n,final} := D_{n,m_n}$ at the first and the final inner iterations, respectively. We have always observed in all ten sets of our data that the first norm $D_{n,first}$ first increases with respect to n, then decreases and attains a unique minimum with respect to $n \in [1, N] = [1, 40]$. On the other hand, the final norm $D_{n,final}$ has either one or two local minima; see Figure 6(a). Let n_1 be the number of the iteration n at which the minimum of the first norms is achieved; e.g., $n_1 = 16$ in Figure 6(a). As the reconstructed coefficient $\epsilon_{rec}(\mathbf{x})$, we first choose $\epsilon_{rec}(\mathbf{x}) := \epsilon_{n_1}(\mathbf{x})$. Next, if $\max_{\overline{\Omega}} \epsilon_{rec}(\mathbf{x}) < 5$ or $\max_{\overline{\Omega}} \epsilon_{rec}(\mathbf{x}) > 10$, then we take the function $\epsilon_{rec}(\mathbf{x})$ as the final reconstruction. Suppose now that $5 \leq \max_{\overline{\Omega}} \epsilon_{rec}(\mathbf{x}) \leq 10$. Then we consider the iteration number n_2 at which the smallest local minimum of the final norm $D_{n,final}$ is achieved, e.g., $n_2 = 33$ in Figure 6(a). Then we take the function $\epsilon_{rec}(\mathbf{x}) := \epsilon_{n_2}(\mathbf{x})$ as the final reconstruction.

As shown in Table 1, the reconstructed refractive indices are quite close to the true values for all dielectric targets. Table 2 shows that reconstructed "appearing" dielectric constants of metallic targets are always in the required range (2.5). However, the shapes and sizes of the targets were not well reconstructed, particularly

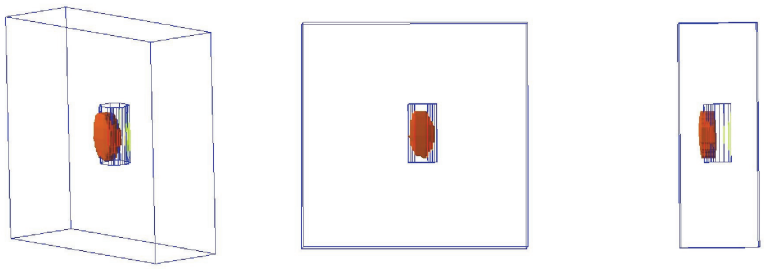

(a) Target 4, 3-d view. (b) Target 4, xy view. (c) Target 4, yz view.

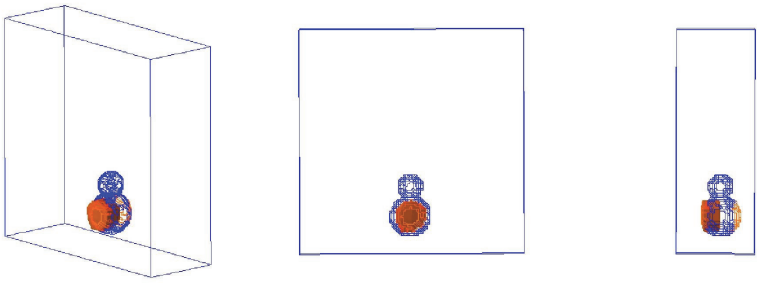

(d) Target 10, 3-d view. (e) Target 10, xy view. (f) Target 10, yz view.

FIG. 7. *Some reconstruction results of Test* 1. *xy view means the projection of the target on the xy plane. yz view means the projection of the target on the yz plane. Thin lines indicate correct shapes.*

the "depth" in the z-direction. To improve this, we use the following postprocessing procedure. Let $P_{z_0} := \{z = z_0\}$ be the plane where the function $\epsilon_{rec}(\mathbf{x})$ achieves its maximal value. Then we compute the truncated coefficient function $\tilde{\epsilon}_{rec}(\mathbf{x})$ as

$$\tilde{\epsilon}_{rec}(\mathbf{x}) = \begin{cases} \epsilon_{rec}(\mathbf{x}) & \text{if } \epsilon_{rec}(x,y,z_0) > \gamma \max \epsilon_{rec}(x,y,z_0), \\ 1 & \text{otherwise,} \end{cases} \tag{4.6}$$

where γ is a truncation factor chosen such that the area of $\{\widetilde{\epsilon}(x,y,z_0) > 1\}$ is the same as that of Γ_T; see (4.2) for Γ_T. Finally, we approximate the depth in the z-direction by truncating $\tilde{\epsilon}_{rec}(\mathbf{x})$ by 90% of its maximal value. This truncation value is chosen based on the trial-and-error tests with nonblind targets. Figure 7 shows imaging results for targets 4 and 10.

4.6. Test 2. In this test, we chose the mesh size of 0.01 by 0.01 by 0.01 in order to represent the targets' shapes more accurately. We use information about the targets in our data preprocessing to restrict the estimated coefficient ϵ in a subdomain of Ω and to choose the first tail function. More precisely, for each target, let $x_{t,min} = \min\{x \in \Gamma_T\}$, $x_{t,max} = \max\{x \in \Gamma_T\}$. The numbers $y_{t,min}$ and $y_{t,max}$ are defined similarly. Then, we define the extended projection by

$$\Gamma_{T,ext} = \{x_{t,min} - 0.03 \le x \le x_{t,max} + 0.03,\ y_{t,min} - 0.03 \le y \le y_{t,max} + 0.03\}.$$

Moreover, denote by $z_{t,front}$ the estimated location of the front side of the target in the z-direction. We then define the following domain $\Omega_{T,ext}$:

$$\Omega_{T,ext} := \{\mathbf{x} \in \Omega : (x,y) \in \Gamma_{T,ext},\ -0.1 \le z \le z_{t,front}\}.$$

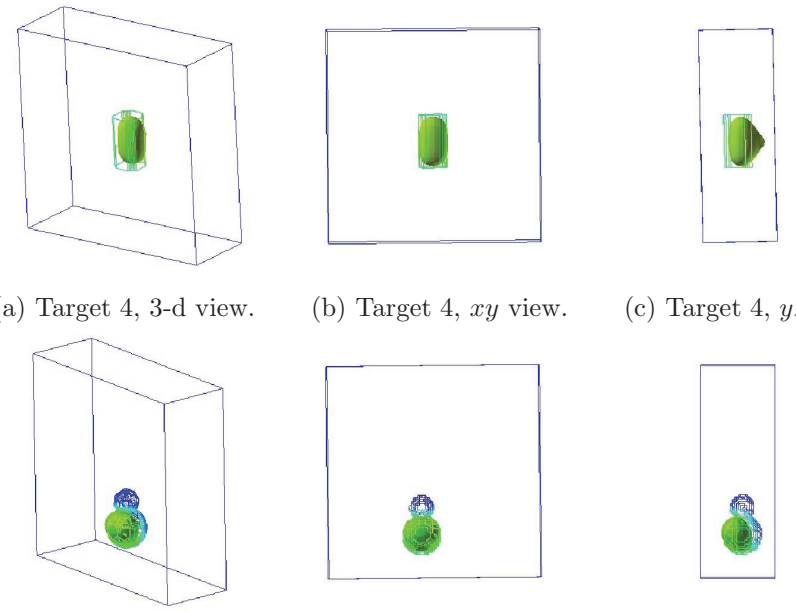

(a) Target 4, 3-d view. (b) Target 4, xy view. (c) Target 4, yz view.

(d) Target 10, 3-d view. (e) Target 10, xy view. (f) Target 10, yz view.

FIG. 8. *Some reconstruction results of Test* 2. *Thin lines indicate correct shapes.*

Clearly, $\Omega_{T,ext} \subset \Omega$. Moreover, this domain should contain the unknown target we are looking for. Next, we chose the first tail function V_0 as the function (2.10), where the function $w(\mathbf{x}, \overline{s})$ is the Laplace transform (2.6) at $s = \overline{s}$ of the solution of the forward problem (2.19)–(2.24) with the coefficient $\epsilon = \epsilon_0$, where

$$\epsilon_0(\mathbf{x}) = \epsilon_u \text{ for } \mathbf{x} \in \Omega_{T,ext}, \qquad \epsilon_0(\mathbf{x}) = 1 \text{ for } \mathbf{x} \notin \Omega_{T,ext}.$$

Moreover, the coefficient is truncated by

$$\epsilon_{n,i}(\mathbf{x}) = \begin{cases} \epsilon_{n,i}(\mathbf{x}) & \text{if } \mathbf{x} \in \Omega_{T,ext} \text{ and } 1 \le \epsilon_{n,i}(\mathbf{x}) \le \epsilon_u, \\ 1 & \text{if } \epsilon_{n,i}(\mathbf{x}) < 1, \\ \epsilon_u & \text{if } \epsilon_{n,i}(\mathbf{x}) > \epsilon_u. \end{cases} \tag{4.7}$$

In this paper, we chose ϵ_u to be 10 for nonmetallic targets and 20 for metallic ones.

Stopping criterion. In this test, the inner iterations were stopped using the same criterion as in Test 1. However, we also set the maximum number of inner iterations to be 5. That means that the inner iterations were stopped if either (4.4) or (4.5) was satisfied for $i < 5$, or if $i = 5$.

Concerning the outer iterations, we have observed that the error $D_{n,final}$ decreased with respect to n first, and then increased after reaching a minimum; see Figure 6(b). At that minimum, the estimated coefficient was a good approximation of the true one for some nonblind targets. Therefore, we stopped the algorithm when this error function attained the minimum.

We have observed through our tests that the shapes of the targets are quite well reconstructed. Figure 8 shows the results of targets 4 and 10 using Test 2. For target 10, we again obtained the lower part, which was filled with the sand; see Figure 5(c)

for its xy projection estimated from the data (recall that air was inside the wooden cover in the upper part of that target).

4.7. Summary of reconstruction results. To compare our computational results with true ones, we have directly measured a posteriori refractive indices $n = \sqrt{\epsilon}$ of dielectric targets. In Tables 1 and 2, the computed values of the refractive index n^{comp} of dielectrics (respectively, *effective* dielectric constant ϵ^{comp} of metals) were chosen as the square root of the maximal values (respectively, the maximal values) of the reconstructed coefficient. Table 1 lists both computed n^{comp} and directly measured refractive indices n of dielectric targets for both Test 1 and Test 2. This table also shows the measurement error in direct measurements of n. Table 2 lists computed "appearing" dielectric constants ϵ^{comp} of metallic targets. We see from Tables 1 and 2 that $\left(n^{\text{comp}}\right)^2 < 5$ for all dielectric targets, while $\epsilon^{\text{comp}} > 13.56$ for all metallic targets in Test 1 and $\epsilon^{\text{comp}} \geq 7.59$ in Test 2. Thus, our algorithm can differentiate quite well between dielectric and metallic targets.

It can be seen from Table 1 that both tests image refractive indices of both blind and nonblind dielectric targets with only a few percent of error, which is even smaller than the error of direct measurements. The average error of computed refractive indices n^{comp} in Tests 1 and 2 is respectively three and seven times less than the average error of direct measurements. Test 1 obtains higher effective dielectric constants of some metallic targets than does Test 2. However, Test 2 provides better shapes.

Unlike targets 1–7, which are homogeneous, targets 8, 9, and 10 are heterogeneous. Target 8 is a wooden doll with air inside. Target 9 is that doll with a piece of metal inside; i.e., this is a metal covered by a dielectric. We can see that only the metal was imaged, because its reflection is much stronger than that of the wood. Target 10 is the same doll partially filled with sand inside (except at the top); i.e., this is one dielectric covered by another one. One can see that only the part with the sand was imaged in target number 10, since its dielectric constant is higher than the air inside the top. Moreover, the reconstructed refractive index is about the average of those of the wood and the sand.

In conclusion, we can see from our tests that, with the proposed data preprocessing procedure, the globally convergent algorithm can image quite well both geometries and materials of the targets in our experimental data even though there is a huge misfit between these data and simulations. Moreover, it can image large inclusion/background contrasts, the case that is well known to be difficult for conventional least-squares approaches.

Appendix. Proof of Theorem 3.1. Consider the function $W(\mathbf{x},\tau) = u^r(\mathbf{x},\tau) - F(\mathbf{x},\tau)$. Define

$$\overline{F}(\mathbf{x},\tau) = \left(\Delta - \partial_\tau^2\right) F. \tag{A.1}$$

Then (3.1)–(3.7) imply that

$$W_{\tau\tau} - \Delta W = \overline{F}(\mathbf{x},\tau), \tag{A.2}$$

$$W(\mathbf{x},0) = W_\tau(\mathbf{x},0) = 0, \tag{A.3}$$

$$\left(\partial_\nu W + W_\tau\right)|_{\Gamma_b \times (0,T)} = 0, \tag{A.4}$$

$$W|_{\Gamma_m \times (0,T)} = 0, \tag{A.5}$$

$$\partial_\nu W|_{\Gamma_3 \times (0,T)} = 0. \tag{A.6}$$

Multiplying both sides of (A.2) by $2W_\tau$, we have

$$2W_\tau W_{\tau\tau} - 2W_\tau \Delta W = \partial_\tau \left(W_\tau^2\right) + \partial_\tau \left(\nabla W\right)^2 - \left(2W_\tau W_x\right)_x - \left(2W_\tau W_y\right)_y - \left(2W_\tau W_z\right)_z$$
$$= 2W_\tau \overline{F}.$$

Let $\widetilde{\tau} \in (0,T)$ be an arbitrary number and $Q_{\widetilde{\tau}} = D \times (0,\widetilde{\tau})$. Integrating the latter equality over $Q_{\widetilde{\tau}}$ and using (A.3), (A.5), and (A.6), we obtain

(A.7)
$$\iint_D \left[W_\tau^2 + \left(\nabla W\right)^2\right](\mathbf{x},\widetilde{\tau})\, d\mathbf{x} - 2\iint_{\Gamma_b \times (0,\widetilde{\tau})} W_\tau \partial_\nu W\, dxdyd\tau = 2\iint_{Q_{\widetilde{\tau}}} W_\tau \overline{F} d\mathbf{x} d\tau.$$

It follows from (A.4) that $-2W_\tau \partial_\nu W = 2W_\tau^2$ for $(\mathbf{x},\tau) \in \Gamma_b \times (0,T)$. Hence, (A.7) implies that

(A.8)
$$\iint_D \left[W_\tau^2 + \left(\nabla W\right)^2\right](x,\widetilde{\tau})\, d\mathbf{x} \le 2\iint_{Q_{\widetilde{\tau}}} W_\tau \overline{F} d\mathbf{x} d\tau \le \iint_{Q_{\widetilde{\tau}}} W_\tau^2 d\mathbf{x} d\tau + \iint_{Q_{\widetilde{\tau}}} \overline{F}^2 d\mathbf{x} d\tau.$$

Define $Z(\tau) = \iint_D [W_\tau^2 + \left(\nabla W\right)^2](\mathbf{x},\tau)\, d\mathbf{x}$. Then (A.8) implies that

$$Z(\widetilde{\tau}) \le \int_0^{\widetilde{\tau}} Z(\tau)\, d\tau + \left\|\overline{F}\right\|^2_{L_2(Q_{\widetilde{\tau}})} \qquad \forall \widetilde{\tau} \in (0,T). \tag{A.9}$$

Now (3.8) follows immediately from (A.9), (A.1), and Gronwall's inequality. ∎

Acknowledgments. The authors are grateful to Mr. Steven Kitchin for his excellent work on data collection. We also thank the anonymous referees for their valuable and stimulating comments and suggestions.

REFERENCES

[1] F. Assous, M. Kray, and F. Nataf, *Time-reversed absorbing conditions in the partial aperture case*, Wave Motion, 49 (2012), pp. 617–631.
[2] A. B. Bakushinsky and M. Yu. Kokurin, *Iterative Methods for Approximate Solution of Inverse Problems*, Springer, Dordrecht, The Netherlands, 2004.
[3] L. Beilina, *Energy estimates and numerical verification of the stabilized domain decomposition finite element/finite difference approach for the Maxwell's system in time domain*, Central European J. Math., 11 (2013), pp. 702–733.
[4] L. Beilina and M. V. Klibanov, *Reconstruction of dielectrics from experimental data via a hybrid globally convergent/adaptive inverse algorithm*, Inverse Problems, 26 (2010), 125009.
[5] L. Beilina and M. V. Klibanov, *Approximate Global Convergence and Adaptivity for Coefficient Inverse Problems*, Springer, New York, 2012.
[6] L. Beilina and M. V. Klibanov, *A new approximate mathematical model for global convergence for a coefficient inverse problem with backscattering data*, J. Inverse Ill-Posed Probl., 20 (2012), pp. 513–565.
[7] L. Beilina and M. V. Klibanov, *Relaxation property for the adaptivity for ill-posed problems*, Appl. Anal., 93 (2014), pp. 223–253.
[8] L. Beilina, K. Samuelsson, and K. Åhlander, *Efficiency of a hybrid method for the wave equation*, in Finite Element Methods, Gakuto Internat. Ser. Math. Sci. Appl. 15, Gakkotosho, Tokyo, 2001.
[9] M. I. Belishev, *Recent progress in the boundary control method*, Inverse Problems, 23 (2007), pp. R1–R67.
[10] A. L. Bukhgeim and M. V. Klibanov, *Uniqueness in the large of a class of multidimensional inverse problems*, Soviet Math. Dokl., 17 (1981), pp. 244–247.
[11] G. Chavent, *Nonlinear Least Squares for Inverse Problems. Theoretical Foundations and Step-by-Step Guide for Applications*, Springer, New York, 2009.

[12] H. W. Engl, M. Hanke, and A. Neubauer, *Regularization of Inverse Problems*, Kluwer Academic Publishers, Dordrecht, The Netherlands, 1996.
[13] B. Engquist and A. Majda, *Absorbing boundary conditions for numerical simulation of waves*, Proc. Natl. Acad. Sci. USA, 74 (1977), pp. 1765–1766.
[14] M. Fink, *Time reversed acoustics*, Physics Today, 50 (1997), pp. 34–40.
[15] M. V. Klibanov, M. A. Fiddy, L. Beilina, N. Pantong, and J. Schenk, *Picosecond scale experimental verification of a globally convergent algorithm for a coefficient inverse problem*, Inverse Problems, 26 (2010), 045003.
[16] A. V. Kuzhuget, L. Beilina, M. V. Klibanov, A. Sullivan, L. Nguyen, and M. A. Fiddy, *Blind backscattering experimental data collected in the field and an approximately globally convergent inverse algorithm*, Inverse Problems, 28 (2012), 095007.
[17] O. A. Ladyzhenskaya, *The Boundary Value Problems of Mathematical Physics*, Springer-Verlag, New York, 1985.
[18] G. Lerosey, J. de Rosny, A. Tourin, and M. Fink, *Focusing beyond the diffraction limit with far-field time reversal*, Science, 315 (2007), pp. 1120–1122.
[19] M. Pastorino, *Microwave Imaging*, John Wiley & Sons, Hoboken, NJ, 2010.
[20] M. Soumekh, *Synthetic Aperture Radar Signal Processing*, John Wiley & Sons, New York, 1999.
[21] WavES Project, *description and software package*, available online at http://waves24.com.
[22] O. Yilmaz, *Seismic Data Imaging*, Society of Exploration Geophysicists, Tulsa, OK, 1987.